HHS Public Access

Author manuscript

Clin Cancer Res. Author manuscript; available in PMC 2020 February 15.

Published in final edited form as:

Clin Cancer Res. 2019 February 15; 25(4): 1331–1342. doi:10.1158/1078-0432.CCR-18-1846.

Whole-body imaging of cell death provides a systemic, minimally invasive, dynamic and near-real time indicator for chemotherapeutic drug toxicity

Steven E. Johnson[1], **Andrey Ugolkov**[2], **Chad R. Haney**[3], **Gennadiy Bondarenko**[2], **Lin Li**[4], **Emily A. Waters**[4], **Raymond Bergan**[2,‡], **Andy Tran**[1], **Thomas V. O'Halloran**[5], **Andrew Mazar**[6,§], and **Ming Zhao**[1,5]

[1]Department of Medicine, Feinberg School of Medicine, Northwestern University

[2]Division of Hematology/Oncology, Feinberg School of Medicine, Northwestern University

[3]Center for Advanced Molecular Imaging, Northwestern University

[4]Depatment of Pathology, Feinberg School of Medicine, Northwestern University

[5]Department of Chemistry, Northwestern University

[6]Department of Pharmacology, Feinberg School of Medicine, Northwestern University

[‡] Current affiliation: Division of Hematology and Medical Oncology, Oregon Health & Science University, Knight Cancer Institute

[§] Current affiliation: Monopar Therapeutics, Inc

Abstract

Purpose: Response to toxicity in chemotherapies vary considerably from tissue to tissue and from patient to patient. An ability to monitor the tissue damage done by chemotherapy may have a profound impact on treatment and prognosis allowing for a proactive management in understanding and mitigating such events. For the first time, we investigated the feasibility of using whole-body imaging to map chemotherapeutic drug-induced toxicity on an individual-basis.

Experimental design: In a preclinical proof-of-concept, rats were treated with a single clinical dose of cyclophosphamide, methotrexate or cisplatin. *In vivo* whole-body imaging data were acquired using ^{99m}Tc-duramycin which identifies dead and dying cells as an unambiguous marker

Authors of correspondence: Andrew Mazar, PhD, Monopar Therapeutics, Inc., 5 Revere Dr., Suite 200, Northbrook, IL, 60062. Phone: 1-847-467-0942. a-mazar@northwestern.edu. Ming Zhao, PhD, Department of Medicine, Tarry 14-753, 300 Superior Street, Feinberg School of Medicine, Northwestern University, Chicago, IL, 60611. Phone: 1-312-503-3226. m-zhao@northwestern.edu.

Authors' Contributions

Conception and design: S.E. Johnson, R. Bergan, A. Mazar, M. Zhao

Development of methodology: S.E. Johnson, A. Ugolkov, C.R. Haney, G. Bondarenko, L. Lin, E.A. Waters, M. Zhao

Acquisition of data: S.E. Johnson, A. Ugolkov, C.R. Haney, G. Bondarenko, L. Lin, E.A. Waters, A. Tran, M. Zhao

Analysis and interpretation of data (e.g., statistical analysis, biostatistics, computational analysis): S.E. Johnson, A. Ugolkov, C.R. Haney, G. Bondarenko, L. Lin, E.A. Waters, R. Bergan, A. Tran, A. Mazar, M. Zhao

Writing, review, and/or revision of the manuscript: S.E. Johnson, A. Ugolkov, G. Bondarenko, L. Lin, R. Bergan, A. Mazar, M. Zhao

Administrative, technical, or material support (i.e., reporting or organizing data, constructing databases): S.E. Johnson, A. Ugolkov, G. Bondarenko, A. Mazar, M. Zhao

Study supervision: A. Mazar, M. Zhao

Conflict of interest statement: The authors have declared that no conflict of interest.

for tissue injury in susceptible organs. Imaging results were cross-validated using quantitative *ex vivo* measurements and histopathology and compared to standard blood and serum panels for toxicology.

Results: The *in vivo* whole-body imaging data detected widespread changes, where spatially-heterogeneous toxic effects were identified across different tissues, within substructures of organs, as well as among different individuals. The signal changes were consistent with established toxicity profiles of these chemotherapeutic drugs. Apart from generating a map of susceptible tissues, this *in vivo* imaging approach was more sensitive compared to conventional blood and serum markers used in toxicology. Also, repeated imaging during the acute period after drug treatment captured different kinetics of tissue injury among susceptible organs in males and females.

Conclusions: This novel and highly translational imaging approach shows promise in optimizing therapeutic decisions by detecting and managing drug toxicity on a personalized basis.

Keywords

drug toxicity; chemotherapy; apoptosis; necrosis; imaging

INTRODUCTION

The success of personalized anticancer therapy depends on optimizing tumor kill and minimizing adverse side effects. Toxicity to normal tissues is a major limitation of chemotherapies; and the susceptibility to drug-induced side effects varies considerably from tissue to tissue and from patient to patient (1–11). Currently the detection of toxicity relies on the presentation of clinical symptoms, which are largely descriptive and qualitative. Toxicity-induced tissue injury can sometimes be asymptomatic until manifested as late-stage organ failure. To address this significant challenge, the current effort presented herein pursues the development of an imaging-based survey by detecting the molecular signatures of tissue injury in response to cytotoxic drugs. This novel approach provides quantitative spatiotemporal information in a minimally invasive and whole-body fashion, and thus identifies the effects of toxicity personally on an existing therapy or a new potential drug candidate.

Pathologically, elevated cell death in the forms of apoptosis and necrosis is an important manifestation of terminal cellular response in toxicity-induced tissue injuries (12–16). Compared to stress-based responses and metabolic changes, a propensity for increased cell death confers an unambiguous marker for toxic side effects of a drug. As such, the whole-body imaging of cell death stands as an unexplored and innovative approach to assessing drug toxicity in a systemic manner.

Aminophospholipids, including phosphatidylserine (PS) and phosphatidylethanolamine (PE), are well-established markers for cell death (17–19). These phospholipids are components of the cell membrane and are sequestered inside a viable cell. When a cell loses viability PS and PE become accessible from the extracellular space presenting an opportunity for detection using aminophospholipid-binding imaging agents (20). In prior

studies, we and others have shown that focal cell death was detectable *in vivo*, for instance in models of tissue injury induced by high-dose x-ray and tumor necrosis factor-α, which are potent apoptosis-inducing treatments (21–24). However, the feasibility of surveying drug toxicity-induced tissue injury at clinically relevant dosages remains to be established, where signal changes may be heterogeneous and pervasive. If proven, such a capability will be critical to achieving a significant breakthrough in bringing this imaging approach to the realm of practicality and ultimately benefits anticancer therapies. For the proof-of-feasibility, the current studies employed ^{99m}Tc-duramycin which is a PE-specific radiopharmaceutical for imaging cell death (22). Comparatively, although Annexin V, a PS-binding protein, has also been widely reported as an imaging agent, we select ^{99m}Tc-duramycin because it has a more favorable biodistribution profile and faster blood clearance for whole-body imaging (25,26).

The primary goal of this study was to examine this whole-body scan as a novel approach for detecting anticancer drug toxicity-induced tissue injury. Our central hypothesis was that the signal changes induced by anticancer drugs at a clinically relevant dose are detectable and reflect the systemic toxicity profile of a cytotoxic drug. Studies were conducted using a rat model, treated with chemotherapeutics with known end-organ toxicity profiles, including cyclophosphamide, methotrexate and cisplatin. These drugs were selected based on their distinct mechanisms of action and toxicity profiles – cyclophosphamide is an alkylating agent that covalently modifies DNA (27); methotrexate primarily inhibits dihydrofolate reductase (28); and cisplatin interferes with DNA replication by forming intra-strand DNA crosslink adducts (29). It was anticipated that this approach would enable the detection and evaluation of tissue injury caused by different cytotoxic drugs since cell death is a common manifestation of terminal cellular response independent of drug pharmacology. *In vivo* single-time point imaging studies were conducted with cross-validation using quantitative *ex vivo* measurements and histopathological analyses. Findings from this new approach were also compared to conventional serum and metabolic panels. Lastly, as a proof-of-concept, we demonstrated in a multi-time point dynamic study using cyclophosphamide that the spatiotemporal kinetics of drug-induced tissue injury could be monitored in the whole body in near-real time.

MATERIALS AND METHODS

Chemotherapeutic Dosing Of Animals

Cyclophosphamide was obtained from Sigma Aldrich and reconstituted to a concentration of 200 mg/mL in saline. Methotrexate was obtained from Enzo Life Sciences and reconstituted to a concentration of 25–40 mg/mL in saline. Cisplatin was purchased from Biorbyt Ltd and reconstituted to a concentration of 2 mg/mL in saline.

The animal protocol was approved by the Institutional Animal Care and Use Committee under the National Institutes of Health guideline. Male rats, of Sprague Dawley (SD) outbred strain, 8–12 weeks of age with a body weight between 250 and 300 g each were administered with each of the chemotherapeutics either intraperitoneally (i.p.) or intravenously (i.v.).

In Vivo Single-Time Point Studies

We conducted a series of single time point *in vivo* imaging studies to test a sub-hypothesis that the changes in ^{99m}Tc-duramycin uptake in tissues in response to cytotoxic drugs were significant and detectable systemically in live animals. The single time point studies were terminal to allow immediate tissue retrieval for cross-validation using histopathological analyses. In addition, the *in vivo* data were cross-validated with quantitative *ex vivo* biodistribution study. The *in vivo* imaging studies were conducted on day-2 after cyclophosphamide treatment (n = 15), day-1 for methotrexate (n = 15), and day-5 for cisplatin (n = 15). The time points were selected as the peak of signal changes for most tissues in a small-scale time series pilot study.

At the designated time, each animal was anaesthetized under 2% isoflurane, secured to a dedicated cradle to allow proper coregistration of imaging data, and injected with ^{99m}Tc-duramycin at approximately 74 MBq of radioactivity via a tail vein catheter. Duramycin was radiolabeled as previously described (22), using approximately 70–125 MBq of ^{99m}Tc-pertechnetate.

MRI

Magnetic Resonance Imaging for anatomical localization was performed on a 9.4T Bruker Biospec MRI system with 30 cm bore, using a 12 cm gradient insert and 72 mm quadrature volume radiofrequency coil (Bruker Inc., Billerica, MA). The rat was anesthetized using isoflurane (3% for induction, 1.5–2% for maintenance) and positioned in an animal bed. Respiration and temperature were monitored using an MRI-compatible small animal monitoring system (Small Animal Instruments, Inc., Stonybrook, NY). A laser positioning system was used to center the thorax of the rat in the magnet. Three consecutive stacks of respiratory gated axial T2 weighted accelerated spin echo (TurboRARE) images were acquired using the following parameters: TR/TE=1000 ms/20 ms, RARE factor 8, field of view 6 cm x 6 cm, 2 mm slice thickness, 1 average, and with fat suppression. A sagittal image (used to aid in segmenting the thymus) was acquired with identical parameters except that there were 13 slices with thickness 1 mm. The positioning system was then used to move the bed 5 cm into the magnet, and the axial imaging stacks were repeated on the abdomen.

Data were exported from Paravision 6 into DICOM format, and imported into Amira 6 to assemble the final MRI volume. The consecutive slice packages in the thorax and abdomen were concatenated, then the thoracic and abdominal stacks were merged after translating the abdominal stack by 5 cm to account for repositioning of the rat. After completion of MRI, the animal bed was transferred intact to the SPECT/CT imaging system.

SPECT/CT acquisition

SPECT was acquired on a U-SPECT^{+}/CT (MILabs, Netherlands) using a general-purpose rat/mouse collimator with 1.5mm pinholes, 1.1mm resolution, and >1500 cps/MBq sensitivity. Two 20 minute sets of data (frames) were acquired and combined. Pixel-based ordered subset expectation maximization (POSEM) reconstruction was used with 4 subsets, 6 iterations, and a 3D-Gaussian kernel (FWHM of 0.8 mm) filter. Voxel size was 0.4 mm^3.

X-ray microCT was used for anatomic guidance and attenuation correction. The collimator was calibrated with a ^{99m}Tc point source to enable conversion from cps to MBq. CT was converted to Hounsfield units for attenuation correction. The data were presented as absolute radioactivity uptake (%ID/cm^3) and fold change over the mean of the control group.

Histology

After imaging data acquisition for the single-time point studies, animals were immediately euthanized. Tissues and organs were excise and portions of fresh tissue specimens were immediately fixed in 4% formaldehyde in phosphate buffer. The tissues were paraffin-embedded, and 4-μm sections were prepared. Tissue slides were analyzed using hematoxylin and eosin (H&E) staining and for the presence of apoptosis using the terminal deoxynucleotidyl transferase-mediated dUTP nick-end labeling (TUNEL) assay and read by 3 qualified pathologists (A.U., G.B., L.L.). TUNEL assay was performed following a standard staining protocol provided by the manufacturer (Roche). The frequency of apoptosis was calculated as an apoptotic index, in which the proportion of cells undergoing apoptosis was expressed as a percentage of all cells. The apoptotic index was calculated as the number of TUNEL-positive cells and bodies per 5000 cells counted in five randomly selected fields in each tissue specimen.

Ex vivo Biodistribution Studies

For biodistribution studies, each group of animals were treated with a single dose of cyclophosphamide (80 mg/kg, i.p., n = 15), methotrexate (100 mg/kg, i.v., n = 15) or cisplatin (2 mg/kg, i.p., n = 15). On day 2, 1 or 5 after the administration of cyclophosphamide, methotrexate or cisplatin, respectively, each animal was injected intravenously with ^{99m}Tc-duramycin (10 – 37 MBq) and were euthanized at 1 hour after ^{99m}Tc-duramycin injection. Organs and tissues were collected for γ-counting. Uptake values were corrected for decay and the radioactivity uptake was expressed as percentage of injected dosage per gram (%ID/g). The data were presented as absolute radioactivity uptake (%ID/g) and fold change over the mean of the control group.

In Vivo Dynamic Studies

Baseline SPECT/CT/MRI imaging data were acquired on males and females (8 animals per group) prior to treatment with a single dose of cyclophosphamide (80 mg/kg, i.p.). On days 1, 3, 5 and 7 post-treatment, each of the animals underwent SPECT/CT/MRI scans as described above. The radioactivity uptake in tissues was measured in terms of %ID/voxel and normalized to the baseline level.

Statistics

For each organ/tissue at each time point, the mean and standard deviation of radioactivity uptake in terms of %ID/cm^3 (*in vivo*) or %ID/g (*ex vivo*) was calculated for the cohort. To examine the statistical differences in radioactivity uptake values in each organ/tissue before and after drug treatment in the sing-time point *in vivo* study and the *ex vivo* cross-validation study, and between each of the post-treatment time points and the baseline value in the dynamic *in vivo* study, the two-tailed Student *t* test was used with a *P* value smaller than

0.05 considered statistically significant. The statistical test was also used to determine the significance of difference between the control and treated groups among serological measurements.

RESULTS

In vivo single time point studies.

Cyclophosphamide-induced tissue injury.—A single dose of cyclophosphamide caused widespread signal changes, with key tissues including the kidneys, spleen, pancreas, colon, thymus, and gut. The *in vivo* whole-body imaging approach enabled examinations systemically as well as in anatomical sub-structures within an organ-of-interest. The *in vivo* data after cyclophosphamide treatment are shown in Fig. 1. The numeric data were expressed in two ways. Changes in the absolute uptake of ^{99m}Tc-duramycin per unit tissue [percentage of total injected radioactivity dose per cm^3 (%ID/cm^3)] in cyclophosphamide-treated tissues relative to the mean value of the non-treated control population (Fig. 1A). The *P* values from two-tailed Student t-test between treated and control group are included in Table 1, where $P < 0.05$ is regarded as statistically significant. The numeric data also can be expressed as fold changes in ^{99m}Tc-duramycin uptake in each drug-treated tissue over the mean of control (Fig. 1B). The changes detected by *in vivo* imaging were cross-validated with quantitative *ex vivo* gamma counting measurements (Suppl. Table 1).

The tissues that exhibited greater changes were consistent with the toxicity profile of cyclophosphamide (27, 30–36). For comparison purposes, a list of known adverse effects in response to cyclophosphamide toxicity is included in Suppl. Table 2. The *in vivo* thymus signal was accompanied by a significantly elevated apoptotic index in cyclophosphamide treated animals (0.55% to 1.70%, 3.09 fold increase, Fig. 1C). Prominent *in vivo* signals were observed in bones, in particular at the epiphysis regions. These changes were confirmed by histopathological evaluation of femur H&E sections showing a degeneration of hematopoietic cells in femoral bone marrow obtained from cyclophosphamide-treated animals (Fig. 1D). There was significantly increased medullary signal in the kidneys, which was corroborated with signs of nephrotoxicity including elevated apoptotic index (0.028% to 0.23%, 8.21 fold increase) and histopathological changes of cellular degeneration with focal hemorrhage (Fig. 1E). In the testes, the apoptotic index was elevated from 0.17% to 0.55% (3.23 fold increase), and according to histopathology, adverse changes included reduced number of spermatids and spermatozoa cells, and the degeneration of spermatogenic cells. These effects were consistent with known toxicity of cyclophosphamide on male fertility (32). Changes in the imaging data in the heart reflected signs of cardiotoxicity identified in histopathology, including elevated apoptosis (undetectable in control TUNEL versus 0.03% in cyclophosphamide-treated) and myocardial edema with myocardial degeneration.

It is notable that changes in imaging signals in the liver did not achieve statistical significance in group-based analysis ($P = 0.18$, Table 1). However, the imaging results captured a heterogeneous response in liver toxicity, where some individuals exhibited a greater susceptibility compared to others as seen in clinical oncology cases. This was confirmed via histopathology, where hepatocyte degeneration with focal necrosis was noted

in some but not all animals. This outcome indicated that the current approach may be useful in personalized as well as population-based studies.

Methotrexate-induced tissue injury.—We then treated a second group of animals with methotrexate which has a distinctly different mechanism of action compared to cyclophosphamide. The signal changes in the *in vivo* imaging data after methotrexate treatment (Fig. 2, Table 1) were cross-validated with quantitative *ex vivo* gamma counting (Suppl. Table 1). In the group-based analysis, tissues with the highest signal changes in terms of net ^{99m}Tc-duramycin uptake per unit tissue included the kidneys, colon and spleen (Fig. 2A). In terms of fold elevation (Fig. 2B), tissues with the largest changes included the colon, kidneys, bones, and spleen. The changes in signals were consistent with the known target organ toxicities of methotrexate including myelosuppression, nephrotoxicity, and adverse effects in the digestive system and the immune system (Suppl. Table 2) (37–40). When compared to the cyclophosphamide-treated group, methotrexate treatment resulted in a different toxicity profile. Signal changes in the liver reached statistical significance (P = 0.029, Table 1), which were consistent with pathological evidence including microscopic signs of hepatocytes degeneration and focal necrosis. The imaging data were corroborated with serological data (see below), where liver enzymes alanine transaminase (ALT) and aspartate aminotransferase (AST) were elevated after methotrexate treatment (Suppl. Table 3). The increase in colon signal was associated with an elevated apoptotic index in the TUNEL assay (0.90% to 1.70%, 1.89 fold increase). Using this imaging approach we identified drastically elevated signals in the joints consistent with the occurrence of bone and joint degeneration reported in the methotrexate literature (47). This was validated in histopathological evaluation, which revealed the presence of joint damage and thrombus formation (Fig. 2C). The elevation of imaging signals in the heart reached statistical significance (P = 0.0014, Table 1), which was indicative of myocardial injury. The findings were validated with histopathology, where hyperemia with edema and mild myocardial degeneration were noted. The imaging approach identified significant signal changes in the testes (Table 1). This was consistent with histopathology evidence of tissue degeneration including reduced number of spermatids cells and spermatozoa. The thymus is known to be susceptible to cytotoxic agents and treatments. The imaging data revealed significant signal changes in the thymus (P = 0.0033, Table 1), which correlated with an elevated apoptotic index (0.55% to 1.02%, 1.85 folds). Changes in skin signals were non-uniform throughout the body. Using image-guided localization, we identified significantly elevated apoptosis in positive skin tissues (1.15% to 2.73%, 2.37 fold increase) (Fig. 2D). According to histopathology, adverse changes included edema of dermis and degeneration of hair follicular epithelial cells. The ability to spatially identify tissue injury is critical to the detection and identification of potential toxicological targets susceptible to adverse events. This capability, as may be envisioned, would help better characterize the toxicity profile of a drug and minimize sampling errors in histopathology-based toxicity studies.

Methotrexate is a folic acid antagonist and is known to cause severe gastrointestinal injury in not all but a subpopulation of recipients (46). This was evident in our study: in a group-based analysis the change in gut signal after methotrexate treatment did not reach statistical significance (P = 0.14, Table 1), signs of substantial toxicity were detected on an individual

basis. In the animal which exhibited a significant ^{99m}Tc-duramycin uptake in the intestinal region, we detected an elevation in apoptotic index (0.69% to 11.07%, 16.04 fold increase). In histopathology we observed inflammation of the lamina propria with interstitial and submucosa hyperemia and edema and erosion of surface epithelium. These changes seen in the data were consistent with gastrointestinal toxicity of the drug further demonstrating the usefulness of the imaging approach for identifying individuals suffering more severe adverse effects within a population.

Cisplatin-induced tissue injury.—A third group of animals (n = 15) were treated with a single dose of cisplatin and were imaged at 5 days post-treatment. Increases in ^{99m}Tc-duramycin uptake were observed in tissues known to be susceptible to cisplatin toxicity. The known susceptible tissues for cisplatin toxicity are listed in Suppl. Table 2 (41–45). According to the net uptake of ^{99m}Tc-duramycin (Fig. 3A), the most prominent tissues included the kidneys, gut and skin. Tissues with the highest fold changes (Fig. 3B) included the skin, kidneys, and gut. When compared to cyclophosphamide and methotrexate treated groups, cisplatin treatment resulted in yet a different toxicity profile. The *in vivo* findings were cross-validated with quantitative *ex vivo* gamma counting (Suppl. Table 1). While cyclophosphamide toxicity appeared to primarily affect the medulla of the kidneys consistent with distal toxicity, cisplatin predominantly affected the cortex of the kidneys (Fig. 3C). TUNEL staining revealed significantly elevated apoptosis in the cortex of cisplatin-treated animals (0.028% to 2.34%, 83.57 fold increase). Histopathological analysis identified evidence of cortical epithelial cell degeneration with focal hemorrhage. As shown in Fig. 3D, the imaging results were correlated with histopathology findings included an enlargement of the joint space, edema, hyperemia, hemorrhage and degeneration of cartilage tissues. These changes were accompanied with an increased signal in the bone marrow throughout the skeletal system, including the femur (Fig. 3E), pelvic, and vertebra bodies. The changes were significant and systemic, consistent with the myelosuppressive effect of cisplatin. The ability to image multiple locations will enable more objective conclusion on a potential test subject or patient by minimizing sampling biases. Cisplatin is known to have toxicity to the gastrointestinal system (45). The imaging data identified significant elevation in gut signals (Fig. 3F), which were correlated with an increase in apoptotic index (0.69% to 1.62%, 2.35 fold increase) and histopathological evidence of tissue degeneration, including moderate to severe inflammation of the lamina propria and submucosa with hyperemia and edema.

Hepatotoxicity has not been considered as a significant side effect for cisplatin, which is consistent with the non-significant statistical outcome in imaging results in group-based analysis ($P = 0.53$). However, we identified individuals with substantial elevation in the liver uptake of ^{99m}Tc-duramycin. Histological analyses on such an individual revealed an elevated apoptotic index (0.11% to 0.37%, 3.36 fold increase) in the TUNEL assay and hepatocyte degeneration with focal necrosis in histopathology examination. These findings may reflect species-dependent susceptibility or uncommon cases of hepatotoxicity associated with cisplatin treatment (48).

Comparison with serological standards.—For the three tested drugs, the *in vivo* imaging data were compared with standard serological toxicological panels. Analyses in comprehensive metabolic panels (CMP, Suppl. Table 3) and complete blood panels (CBC, Suppl. Table 4) between control and drug treated groups identified a number of changes which were consistent with manifestations of drug toxicity. Significant lympho/leukopenia was observed likely due to cytotoxicity on circulating white blood cells and the myelosupressive effect on hematopoietic stem cells in the bone marrow. There were indications of nephrotoxicity especially for methotrexate and cisplatin (creatinine elevation, $P = 0.03$ and 0.04, respectively). For cyclophosphamide treatment there was a modest increase in the mean creatinine value compared to control (Suppl. Table 3), but the P value did not reach significance. However, the CMP data identified significantly changes in calcium ($P = 0.02$), chloride ($P = 0.01$) and sodium ($P = 0.03$), which may be indicative of renal distress and electrolyte disturbances. Liver damage was identified among the CMP data in methotrexate-treated group (ALT $P < 0.001$, AST $P = 0.01$); whereas the changes were not statistically significant for cyclophosphamide- and cisplatin-treated groups. The serological findings in liver enzymes were in agreement with the imaging data, where hepatic signal changes were significant after methotrexate treatment ($P = 0.029$), but not cyclophosphamide ($P = 0.18$) or cisplatin ($P = 0.53$). Overall, the serological data and findings from the imaging approach were both corroborative and complementary, where the former provides information on the cellular and metabolic changes, the latter detects spatially specific changes in individual organs and tissues.

In vivo dynamic imaging study after cyclophosphamide treatment.

In an effort to further examine the spatiotemporal utility of this imaging approach, and the ability to assess susceptibility in both sexes, dynamic studies were performed on male and female rats after treatment with cyclophosphamide. We tested the sub-hypothesis that the kinetics of drug toxicity-induced signal changes could be assessed systemically and dynamically by whole-body imaging. This approach involved the acquisition of a baseline scan prior to drug administration, followed by multiple post-treatment scans in male (n = 8) and female (n = 8) rats spanning the acute phase at days 1, 3, 5 and 7. The data from each animal provided dynamic information, which reflected the spatiotemporal distribution of tissue susceptibility to toxicity-induced injury. In addition, this approach presented an advantage where the baseline scan for each animal served as an internal control allowing for the repeated imaging and continuous monitoring of tissue changes with individualized data analysis.

A single dose of cyclophosphamide treatment resulted in widespread changes in ^{99m}Tc-duramycin uptake throughout the body in both males and females, where different tissues not only exhibited different levels of susceptibility, but also differed in the kinetics of signal changes. The changes were relatively consistent between both sexes. Representative images from the males are shown in Fig. 4 to demonstrate the dynamic signal changes in some of the susceptible tissues, including the gut (Fig. 4A), thymus (Fig. 4B), kidneys (Fig. 4C), spleen (Fig. 4D) and bones (knees and femurs, Fig. 4E). The plots of fold changes for males and females are presented in Fig. 5; and the numerical data, including means plus/minus standard deviations and the P values from 2-tailed Student t test, are included in Suppl. Table

5. Visually, the toxicity profiles (Fig. 5) between males and females were remarkably similar. According to the statistical test, tissues that were consistently identified in both sexes to have significant signal changes were bones, brain, colon, fat, heart, kidneys, liver, stomach and thymus. In the female reproduction tract, the ovaries also exhibited statistically significant signal elevation. In addition, the dynamic studies captured different kinetics in signal changes. For instance, the kidneys, skeletal muscles, skin and thymus underwent early changes within 8 hours post-treatment, whereas other tissues including the adipose tissue, bones, heart, liver, spleen and stomach had a delayed response with their signal changes peaking on or after day 3.

DISCUSSION:

The primary aim of this study was to examine the feasibility of using an imaging approach for assessing systemic tissue injury induced by cytotoxic chemotherapeutics. The central hypothesis was that the signal changes in response to drug toxicity can be detectable systemically in an individualized manner. Pharmaceuticals vary in toxicity and therapeutic efficacy as a consequence of mechanisms of action, pharmacodynamics and pharmacokinetics. A minimally invasive approach for detecting adverse effects of a drug on an individualized basis brings value in determining the toxicity profile for a given therapy. The current data demonstrated, using three established chemotherapeutic drugs with distinct toxicity profiles, that tissue injury induced by chemotherapeutic drug treatment at a clinically relevant dose can be detected by *in vivo* imaging in near-real time, where the signal changes are consistent with known adverse effects.

Drug toxicity can be projected with a broad range of manifestations, from changes in molecular interactions, signaling and metabolism to tissue/organismal-level responses such as hormonal and functional dysregulations. Among these, cell death presents a form of terminal and extreme cellular response to toxicity. A significantly elevated level of pathological cell death in a target tissue confers an unambiguous indicator for the susceptibility to the adverse effects of a given drug or treatment.

Systemic toxicity is a highly dynamic and individualized process, where tissue response differs spatially and temporally, and thus each individual may present with a different level of susceptibility (49,50). To the best of our knowledge, the current approach represents the first effort to test the feasibility of delineating toxicity-induced tissue injury in a systemic approach. The minimally-invasive nature allows repeated scans of the same subject both before and after drug treatment at multiple time points. The *in vivo* dynamic data detected variations in the onset and progression of signal changes in different organs and tissues. The imaging data provided a visual map in a whole body fashion, and are particularly useful for identifying problematic sites when changes are regional and heterogeneous. In addition to the spatial heterogeneity within an organ, there are variations in the same tissue among different individuals. Tissues which exhibit the greatest variations in response to drug toxicity from one individual to another are likely contributors to personalized susceptibility. In this respect, the current studies demonstrated the feasibility of a potential approach for delineating the dynamics of tissue injury in a personalized fashion. Compared to histopathology-based toxicity studies, which necessitate euthanizing multiple groups of

animals for full tissue biopsy, the imaging approach provides indications for susceptible tissues in a continuous fashion in near-real time. The prompt availability of such information is complementary to histopathology-based toxicity studies and may help accelerate the decision making process in drug discovery and development. In addition, an imaging approach may be able to detect adverse changes in animals at the tissue level after a single dose of drug, thus improving the ability to compare multiple therapies or drugs for tolerability in a time-efficient way.

The *in vivo* imaging of cell death is conceptually simple, but a major challenge resides in minimizing systemic background and improving target-to-background ratio in order to make it technologically feasible to detect more subtle signal changes that reflect the underlying pathology. In the present study, the use of ^{99m}Tc-duramycin achieved an appreciable level of sensitivity with a reasonable dynamic range which covers both relatively high and low level signal changes. While the molecular mechanism of phospholipid externalization does not differentiate apoptosis from necrosis, being able to detect a marker for tissue injury regardless of the modes or causes of cell death is a desirable advantage. The outcome of the current investigation sets the goals for continued research efforts to develop future generation imaging agents, acquisition techniques and post-processing algorithms, which will be geared toward improving the data quality, which in turn, can lead to greater detection sensitivity.

At the preclinical stage, an *in vivo* approach for assessing toxicity could help address unmet needs in pharmaceutical research and development. Intuitively, a potential role for imaging would be in preclinical toxicity studies, which currently rely on histopathology-based tissue analyses. An effective way to identify injury in intact organs and tissues could provide useful indicators that independently validate or improve upon histopathology findings, particularly when the toxicity effect is heterogeneous and tends to lead to sampling errors during tissue retrieval. A second potential role for an *in vivo* toxicity assessment may fit in the pharmacology phase of drug development, which is relatively early in drug discovery with the comparison of a number of lead candidates. This stage may be too early for full-scale toxicity studies for these candidates, yet timely characterizations of adverse event profiles are essential to reaching a go-no-go decision for these candidates. Given the minimally invasive nature of the *in vivo* approach, it may provide the needed information to guide candidate selection at near-real time. This information on the spatiotemporal occurrence of adverse effects will help select efficacious drug candidates with lower toxicity for prioritization, while eliminating candidates that are too toxic to vital organs/tissues. The ability to prioritize candidates at the pharmacology phase will help eliminate problematic drug candidates early on so that resources can be better focused on bringing the right program forward. In a third potential area, post-marketing surveillance is an important component in pharmacovigilance. Drugs with unforeseen side effects or drug-drug interactions may need to be reassessed for safety especially when they are administered to patients that are on multiple drugs. An *in vivo* dynamic study in a systematic fashion can be useful for identifying problematic side effects and for testing alternative dosing/formulation to mitigate the issue.

The minimally invasive nature of this imaging approach makes it feasible for clinical translation. Ultimately, when fully established for human use, the current approach can conceivably play a role in detecting and managing adverse side effects by providing an objective, quantitative matric for determining toxicity. This capability will identify the onset of tissue injury in both symptomatic and asymptomatic scenarios, thus reduces uncertainties and biases. The early detection of tissue injury in susceptible organs will be helpful in making timely adjustment in therapy to maximize efficacy and reduce the risk of serious adverse effects. The current imaging approach is administered on an individual basis. It is well appreciated that response to drug toxicity is highly variable from tissue to tissue and individual to individual. A way to identify susceptibility to serious side effects in the whole-body fashion provides a unique opportunity to manage cancer therapy on a personalized level.

In conclusion, the current data demonstrated the feasibility of an approach to characterize toxicity-induced tissue injury. Work presented in these studies indicates a new opportunity for the minimally invasive evaluation of systemic drug toxicity by utilizing a molecular biomarker for tissue injury. This approach provides useful information on both individual and population levels for gauging systemic tissue injury induced by chemotherapeutics. The technique has potential to generate a real impact in pharmaceutical development and clinical oncology.

Supplementary Material

Refer to Web version on PubMed Central for supplementary material.

Acknowledgement

The Authors wish to thank the funding support from the National Institutes of Health (5R01 CA185214, 1S10 OD016398, 5R01 HL102085). Technical assistance from Xingyao He is gratefully appreciated.

Financial support: National Institutes of Health (5R01CA185214, 1S10OD016398, 5R01HL102085)

REFERENCES

1. Hait WN, Hambley TW. Targeted cancer therapeutics. Cancer Res. 2009;69:1263–1267. [PubMed: 19208830]
2. Fallowfield LJ, Harper P. Health-related quality of life in patients undergoing drug therapy for advanced non-small-cell lung cancer. Lung Cancer. 2005;48:365–377. [PubMed: 15893006]
3. Sledge GW, Jr. Breast cancer in the clinic: treatments past, treatments future. J Mammary Gland Biol Neoplasia. 2001;6:487–495. [PubMed: 12013537]
4. Jansman FG, Sleijfer DT, Coenen JL, De Graaf JC, Brouwers JR. Risk factors determining chemotherapeutic toxicity in patients with advanced colorectal cancer. Drug Saf. 2000;23:255–278. [PubMed: 11051215]
5. Rousseau A, Marquet P, Debord J, Sabot C, Lachatre G. Adaptive control methods for the dose individualization of anticancer agents. Clin Pharmacokinet. 2000;38:315–353. [PubMed: 10803455]
6. DeMario MD, Ratain MJ. Oral chemotherapy: rationale and future directions. J clin Oncol. 1998;16:2557–2567. [PubMed: 9667278]
7. Iarussi D, Indolfi P, Galderisi M, Bossone E. Cardiac toxicity after anthracycline thermotherapy in childhood. Herz. 2000;25:676–88. [PubMed: 11141677]

8. Walko CM, McLeod HL. Personalizing medicine in geriatric oncology. J Clin Oncol. 2014;32:2581–2586. [PubMed: 25071134]
9. Pachman DR, Watson JC, Loprinzi CL. Therapeutic strategies for cancer treatment related peripheral neuropathies. Curr Treat Options Oncol. 2014;15:567–80. [PubMed: 25119581]
10. Barbolosi D, Ciccolini J, Lacarelle B, Barlesi F, Andre N. Computational oncology-mathematical modeling of drug regimens for precision medicine. Nat Rev Clin Oncol. 2016;13:242–254. [PubMed: 26598946]
11. Bocci G, Kerbel RS. Pharmacokinetics of metronomic chemotherapy: a neglected but crucial aspect. Nat Rev Clin Oncol. 2016;13:659–673. [PubMed: 27184418]
12. Mailloux A, Grenet K, Bruneel A, Beneteau-Burnat B, Vaubourdolle M, Baudin B. Anticancer drugs induce necrosis of human endothelial celsl involving both oncosis and apoptosis. Eur J Cell Biol. 2001;80:442–449. [PubMed: 11484935]
13. Keane MM, Ettenberg SA, Nau MM, Russell EK, Lipkowitz S. Chemotherapy augments TRAIL-induced apoptosis in breast cell lines. Cancer Res. 1999;59:734–741. [PubMed: 9973225]
14. Pritchard DJ, Wright MG, Sulsh S, Butler WH. The assessment of chemically induced liver injury in rats. J Appl Toxicol. 1987;7:229–236. [PubMed: 3624782]
15. Iorga A, Dara L, Kaplowitz N. Drug-induced liver injury: cascade of events leading to cell death, apoptosis or necrosis. Int J Mol Sci. 2017;18.
16. Ryu HY, Emberley JK, Schleziger JJ, Allan LL, Na S, Sherr DH. Environmental chemical-induced bone marrow B cell apoptosis: death receptor-independent activation of a caspase-3 to caspase-8 pathway. Mol Pharmacol. 2005;68:1087–1096. [PubMed: 16014577]
17. Martin SJ, Reutelingsperger CP, McGahon AJ, Rader JA, van Schie RC, LaFace DM, et al. Early redistribution of plasma membrane phosphatidylserine is a general feature of apoptosis regardless of the initiating stimulus: inhibition by overexpression of Bcl-2 and Abl. J Exp Med. 1995;182(5): 1545–56. [PubMed: 7595224]
18. Balasubramanian K, Schroit AJ. Aminophospholipid asymmetry: A matter of life and death. Annu Rev Physiol. 2003;65:701–34. [PubMed: 12471163]
19. Mauilk N, Kagan VE, Tyurin VA, Das DK. Redistribution of phosphatidylethanolamine and phosphatidylserine precedes reperfusion-induced apoptosis. Am J Physiol. 1998;274:H242–248. [PubMed: 9458873]
20. van Meer G Dynamic transbilayer lipid asymmetry. Cold Spring Harb Perspect Biol. 2011;3(5).
21. Blankenberg FG, Katsikis PD, Tait JF, Davis RE, Naumovski L, Ohtsuki K, et al. In vivo detection and imaging of phosphatidylserine expression during programmed cell death. Proc Natl Acad Sci U S A. 1998;95(11):6349–54. [PubMed: 9600968]
22. Zhao M, Li Z, Bugenhagen S. 99mTc-labeled duramycin as a novel phosphatidylethanolamine-binding molecular probe. J Nucl Med. 2008;49:1345–52. [PubMed: 18632826]
23. Johnson SE, Li Z, Liu Y, Moulder JE, Zhao M. Whole-body imaging of high-dose ionizing irradiation-induced tissue injuries using 99mTc-duramycin. J Nucl Med. 2013;54:1397–1403. [PubMed: 23804327]
24. Delvaeye T, Wyffels L, Deleye S, Lemeire K, Gonçalves A, Decrock E, et al. Noninvasive whole-body imaging of phosphatidylethanolamine as a cell death marker using ^{99m}Tc-duramycin during TNF-induced SIRS. J Nucl Med. 2018 2 1.
25. Audi S, Li Z, Capacete J, Liu Y, Fang W, Shu LG, et al. Understanding the in vivo uptake kinetics of a phosphatidylethanolamine-binding agent (99m)Tc-Duramycin. Nucl Med Biol. 2012 8;39(6): 821–5. [PubMed: 22534031]
26. Kawai H, Chaudhry F, Shekhar A, Petrov A, Nakahara T, Tanimoto T, et al. Molecular Imaging of Apoptosis in Ischemia Reperfusion Injury With Radiolabeled Duramycin Targeting Phosphatidylethanolamine: Effective Target Uptake and Reduced Nontarget Organ Radiation Burden. JACC Cardiovasc Imaging. 2018 2 9.
27. Emadi A, Jones RJ, Brodsky RA. Cyclophosphamide and cancer: golden anniversary. Nat Rev Clin Onco. 2009;6:638–647.
28. Rajagopalan PTR, Zhang Z, McCourt L, Dwyer M, Benkovic SJ, Hammes GG. Interaction of dihydrofolate reductase with methotrexate: ensemble and single-molecule kinetics. Proc Natl Acad Sci USA. 2002;99:13481–13486. [PubMed: 12359872]

29. Chvalova K, Brabec V, Kasparkova J. Mechanism of the formation of DNA-protein cross-links by antitumor cisplatin. Nucleic Acid Res. 2007;35:1812–1821. [PubMed: 17329374]
30. Rehman MU, Tahir M, Ali F, Qamar W, Lateef A, Khan R, et al. Cyclophosphamide-induced nephrotoxicity, genotoxicity, and damage in kidney genomic DNA of Swiss albino mice: the protective effect of Ellagic acid. Mol Cell Biochem. 2012;365:119–27. [PubMed: 22286819]
31. Kim J, Chan JJ. Cyclophosphamide in dermatology. Australas J Dermatol. 2017;58:5–17. [PubMed: 26806212]
32. Ghobadi E, Moloudizargari M, Asghari MH, Abdollahi M. The mechanisms of cyclophosphamide-induced testicular toxicity and the protective agents. Expert Opin Drug Metab Toxicol. 2017;13:525–36. [PubMed: 28019118]
33. McCarroll N, Keshava N, Cimino M, Chu M, Dearfield K, Keshava C, et al. An evaluation of the mode of action framework for mutagenic carcinogens case study: Cyclophosphamide. Environ Mol Mutagen. 2008;49:117–31. [PubMed: 18240158]
34. Musiatowicz B, Sulkowska M, Sulik M, Famulski W, Dzieciol J, Sobaniec-Lotowska M, et al. Cyclophosphamide in diffuse lung damage. Rocz Akad Med Bialymst. 1997;24 Suppl 2:73–8.
35. De Jonge ME, Huitema AD, Rodenhuls S, Beijnen JH. Clinical pharmacokinetics of cyclophosphamide. Clin Pharmacokinet. 2005;44:1135–64. [PubMed: 16231966]
36. Fraiser LH, Kanekal S, Kehrer JP. Cyclophosphamide toxicity. Characterising and avoiding the problem. Drugs. 1991;42:781–95. [PubMed: 1723374]
37. Howard SC, McCormick J, Pui CH, Buddington RK, Harvey RD. Preventing and managing toxicities of high-dose methotrexate. Oncologist. 2016;21:1471–82. [PubMed: 27496039]
38. Campbell JM, Bateman E, Stephenson MD, Bowen JM, Keefe DM, Peters MD. Methotrexate-induced toxicity pharmacogenetics: an umbrella review of systematic reviews and meta-analyses. Cancer Chemother Pharmacol. 2016;27:27–39.
39. Ortiz Z, Shea B, Suarez-Almazor ME, Moher D, Wells GA, Tugwell P. The efficacy of folic acid and folinic acid in reducing methotrexate gastrointestinal toxicity in rheumatoid arthritis. A metaanalysis of randomized controlled trials. J Rheumatol. 1998;25:36–43. [PubMed: 9458200]
40. Khan N, Abbas AM, Whang N, Balart LA, Bazzano LA, Kelly TN. Incidence of liver toxicity in inflammatory bowel disease patients treated with methotrexate: a meta-analysis of clinical trials. 2012;18:359–67.
41. Norrgren K, Sjolin M, Bjorkman S, Areberg J, Johnsson A, Johansson L, et al. Comparative renal, hepatic, and bone marrow toxicity of cisplatin and radioactive cisplatin (191Pt) in Wistar rats. Cancer Biother Radiopharm. 2006;21:528–34. [PubMed: 17105425]
42. Miller RP, Tadagavadi RK, Ramesh G, Reeves WB. Mechanism of cisplatin nephrotoxicity. Toxins (Basel). 2010;2:2490–518. [PubMed: 22069563]
43. Astolfi A, Ghiselli S, Guaran V, Chicca M, Simoni E, Olivetto E, et al. Correlation of adverse effects of cisplatin administration in patients affected by solid tumors: a retrospective evaluation. Oncol Rep. 2013;29:1285–92. [PubMed: 23404427]
44. Demkow U, Stelmaszczyk-Emmel A. Cardiotoxicity of cisplatin-based chemotherapy in advanced non-small cell lung cancer patients. Respir Physiol Neurobiol. 2013;187:64–7. [PubMed: 23548823]
45. Stojanovska V, Sakkal S, Nurgali K. Platinum-based chemotherapy: gastrointestinal immunomodulation and enteric nervous system toxicity. Am J Physiol Gastrointest Liver Physiol. 2015;308:G223–32. [PubMed: 25501548]
46. Toquet S, Nguyen Y, Sabbagh A, Djerada Z, Boulagnon C, Bani-Sadr F. Severe apoptotic enteropathy caused by methotrexate treatment for rheumatoid arthritis. Joint Bone Spine. 2016;83:217–9. [PubMed: 26494588]
47. Gnudi S, Butturini L, Ripamonti C, Avella M, Bacci G. The effects of methotrexate on bone. Ital J Orthop Traumatol. 1988;14:227–31. [PubMed: 3220728]
48. Cersosimo RJ. Hepatotoxicity associated with cisplatin chemotherapy. Ann Pharmacother. 1993;27:438–41. [PubMed: 8477119]
49. Moen E, Godley LA, Zhang W, Dolan ME. Pharmacogenomics of chemotherapeutic susceptibility and toxicity. Genome Med. 2012;4:90. [PubMed: 23199206]
50. Grandjean P Individual susceptibility to toxicity. Tox Letters. 1992;64/65:43–51.

Statement of significance:

Toxicity to normal tissues is a significant limitation in chemotherapies. The current work demonstrated an *in vivo* imaging-based approach for characterizing toxicity-induced tissue injury in a systemic, dynamic and near-real time fashion. This novel approach shows promise in optimizing therapeutic decisions by monitoring drug toxicity on a personalized basis.

Statement of translational relevance:

The response to chemotherapeutic drug toxicity is highly variable from tissue to tissue and from individual to individual. The ability to identify susceptibility to serious side effects in the whole-body fashion provides an opportunity to optimize cancer therapy on a personalized level. The minimally invasive nature of this imaging approach makes it feasible for clinical translation, where it can play a role in detecting and managing adverse side effects by providing an objective, quantitative matric for determining toxicity. This capability will identify the onset of tissue injury in both symptomatic and asymptomatic scenarios, thus reducing uncertainties and biases. The early detection of tissue injury in susceptible organs will be helpful in making timely adjustment in therapy to maximize efficacy and reduce the risk of serious adverse effects on a personalized basis.

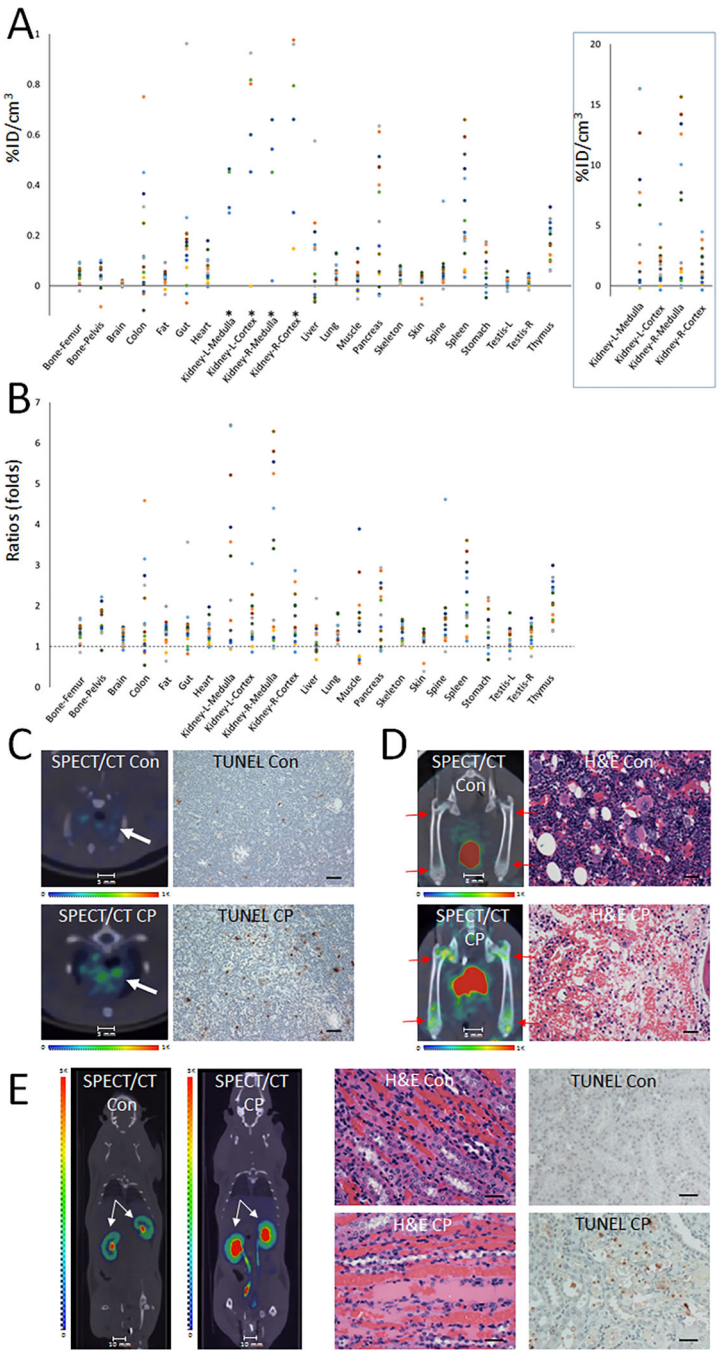

Figure 1.

In vivo single time point study of cyclophosphamide treated rats at 48 hours. A single dose of cytotoxic drug cyclophosphamide (80 mg/kg) caused widespread changes in ^{99m}Tc-duramycin uptake in different organs and tissues. **A)** Scatter plot of net change in radioactivity uptake in terms of percentage of injected dose per cm^3 in cyclophosphamide treated (n = 15) over the mean of nontreated control tissues (n = 15). *Signal changes in the kidney are plotted at a different scale in the box on right. **B)** Scatter plot of fold changes in radioactivity uptake among tissues at 48 hour after cyclophosphamide treatment. A ratio of 1

indicates no change. **C)** SPECT/CT fusion images of thymus (arrows) from control and cyclophosphamide (CP) treated animals. Representative images of TUNEL staining are shown on the right panel (scale bar = 75 μm). **D)** SPECT/CT fusion and corresponding H&E images of the femurs obtained from control and cyclophosphamide-treated animals as indicated. Significant signal elevation was detected in the symphysis of the bones as indicated by arrows. In contrast to control animals, H&E stained section of femoral bone demonstrate the degradation of hematopoietic cells in cyclophosphamide-treated animals (scale bar = 50 μm). **E)** SPECT/CT fusion images of kidney demonstrate an increased radioactivity uptake in cyclophosphamide treated animals. Note the elevated signal intensity particularly in the infundibulum. H&E staining (scale bar = 75 μm) indicated in cyclophosphamide-treated animal the kidney had generalized hyperemia and swelling, with foci of dilated proximal and distal tubules that contained granular eosinophilic deposits with tubular epithelium. Moderate degeneration of tubular epithelial cells with focal vacuolation of the cytoplasm, pyknosis of the nuclei and eosinophilic cast formation were noted. Representative images of TUNEL staining show a significant increase in apoptosis in kidney from cyclophosphamide-treated animal (scale bar = 75 μm).

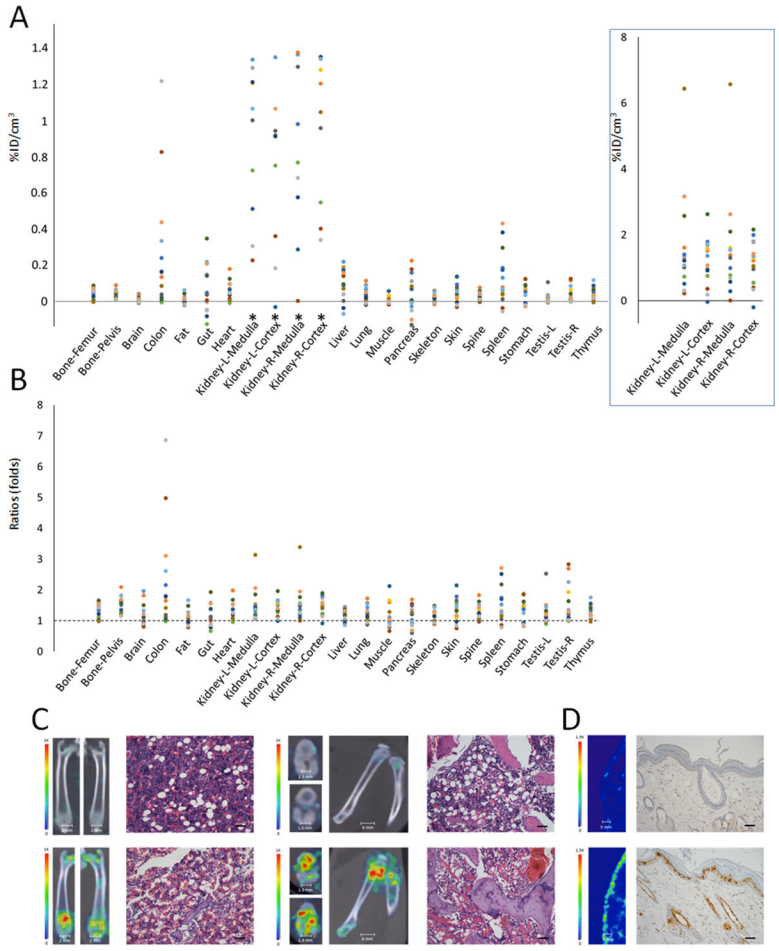

Figure 2.

In vivo single time point study of methotrexate treated rats (100 mg/kg, n = 15) at 24 hours. **A)** Scatter plot of net change in radioactivity uptake in terms of percentage of injected dose per cm^3 in methotrexate treated (n = 15) over the mean of nontreated control tissues (n = 15). *Signal changes in the kidney are plotted at a different scale in the box on right. **B)** Scatter plot of fold changes in radioactivity uptake among tissues. A ratio of 1 indicates no change. **C)** SPECT/CT fusion images of the femurs and knees in control and methotrexate treated animals are presented. Significant signal elevation was detected in the symphysis of the bones and knee joints. H&E stained section of femoral bone demonstrates a depletion of hematopoietic cells in bone marrow of methotrexate-treated animals (scale bar = 75 μm). **D)** SPECT images of skin obtained from the control and methotrexate treated animals with corresponding TUNEL images as indicated (apoptotic nuclei were stained positive with the deposition of brown pigment, scale bar = 75 μm).

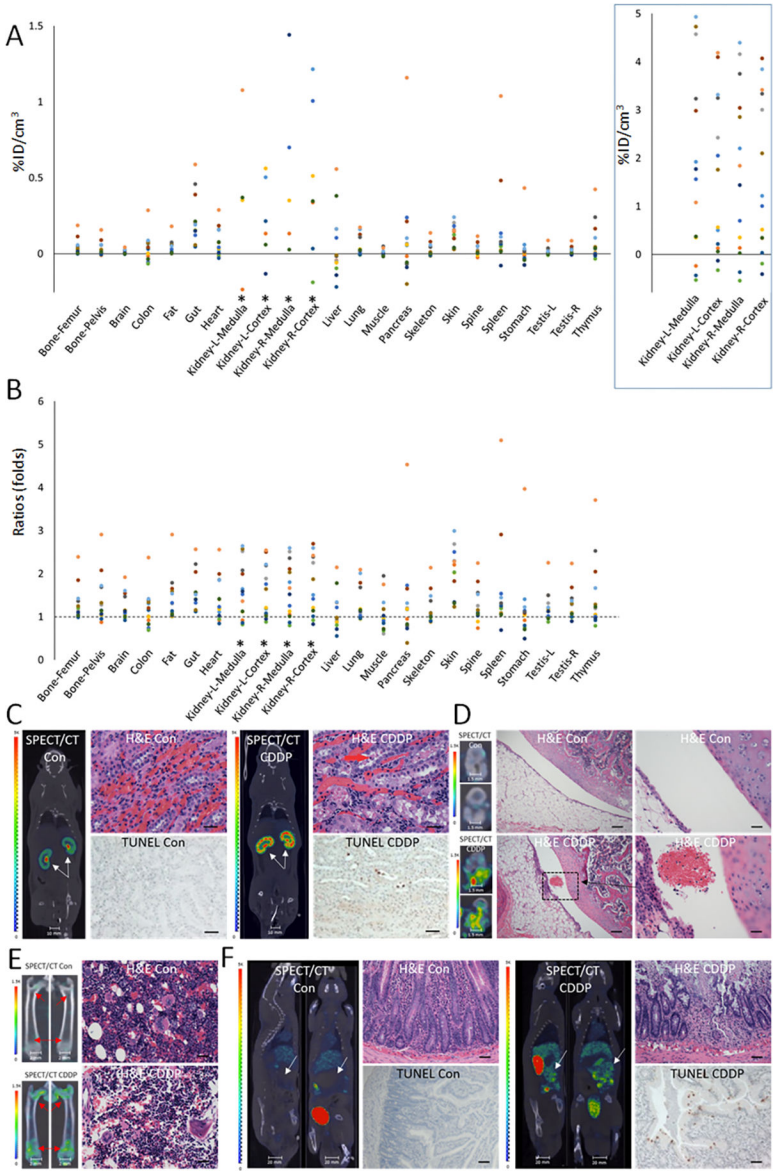

Figure 3.

In vivo single time point study of cisplatin treated rats ((2 mg/kg, n = 15) on day-5. **A)** Scatter plot of net change in radioactivity uptake in terms of percentage of injected dose per cm^3 in cisplatin treated (n = 15) over the mean of nontreated control tissues (n = 15). *Signal changes in the kidney are plotted at a different scale in the box on right. **B)** Scatter plot of fold changes in radioactivity uptake among tissues. A ratio of 1 indicates no change. **C)** SPECT/CT fusion images of kidneys from control and cisplatin (CDDP) treated animals demonstrate an elevated signal intensity in the parenchymal region. The corresponding H&E and TUNEL images are shown (scale bar = 75 μm). **D)** SPECT/CT fusion images of knees from control and cisplatin treated animals demonstrate radioactivity uptake. Corresponding micrographs with H&E staining demonstrate foci of hemorrhage and degeneration of knee joint tissue (left scale bars = 75 μm, right scale bars = 18.75 μm). **E)** Significant signal elevation was detected in the symphysis of femurs. Decreased number of hematopoietic cells

was observed in femoral bone marrow of animals treated with cisplatin as shown by H&E images (scale bar = 75 μm). **F)** SPECT/CT fusion images show the gut region in control and cisplatin treated animals, with corresponding H&E and TUNEL images which demonstrated tissue degeneration and the elevation of apoptosis (scale bar = 75 μm).

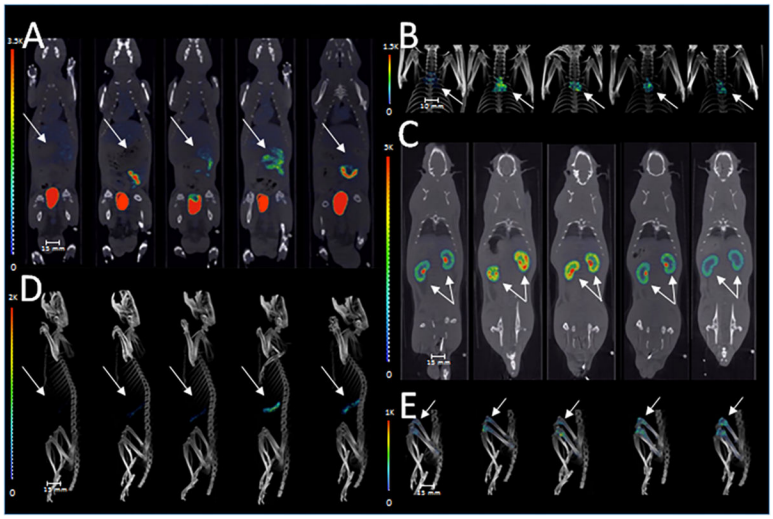

Figure 4.

Dynamic imaging of cyclophosphamide treated rats. Signal changes in representative tissues from male rats before and 1, 3, 5 and 7 days after cyclophosphamide treatment (80 mg/kg, single dose). SPECT/CT fusion images demonstrate signal changes in the gut **(A)**, thymus **(B)**, kidneys **(C)**, spleen **(D)** and femurs/knees **(E)** over the course of 7 days after treatment. Note that the onset and progression of tissue injury differ in a spatiotemporal fashion.

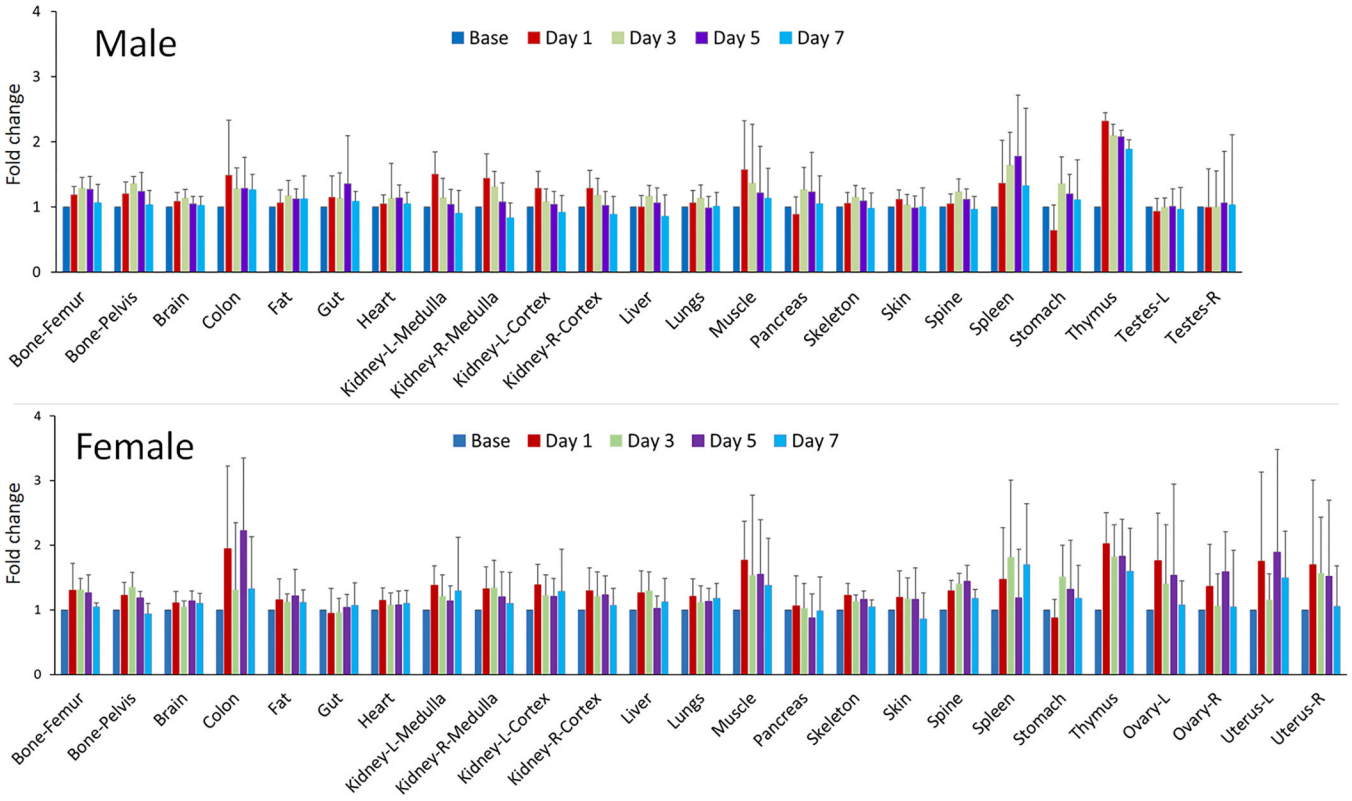

Figure 5.

Relative signal changes in organs/tissues in male and female rats before and at 1, 3, 5 and 7 days after cyclophosphamide treatment (80 mg/kg, single dose). The data are presented as fold change, where the baseline signal intensity in each tissue before cyclophosphamide administration was normalized to 1. Note that the toxicity profiles between the two sexes were visually comparable, where the main susceptible tissues, including the bones, brain, colon, fat, heart, kidneys, liver, stomach and thymus were consistently identified between males and females. Signal changes in the ovaries were also significant as a result of cyclophosphamide treatment.

Table 1.

Statistical comparison between drug-treated and control groups for *in vivo* measurements.

	Control	Cyclophosph-amide	Methotrexate	Cisplatin
Bone-Femur	0.13±0.038	0.18±0.031(0.001)	0.18±0.029(0.006)	0.17±0.053(0.036)
Bone-Pelvis	0.083±0.021	0.13±0.028(<0.0001)	0.12±0.022(<0.0001)	0.11±0.045(0.021)
Brain	0.045±0.008	0.056±0.009(0.0005)	0.052±0.016(0.12)	0.055±0.013(0.021)
Colon	0.21±0.053	0.37±0.23(0.021)	0.46±0.35(0.017)	0.24±0.089(0.26)
Fat	0.094±0.027	0.12±0.03(0.0054)	0.11±0.024(0.20)	0.13±0.048(0.013)
Gut	0.38±0.16	0.55±0.24(0.020)	0.46±0.14(0.14)	0.59±0.16(0.0011)
Heart	0.19±0.050	0.25±0.051(0.0007)	0.25±0.048(0.0014)	0.26±0.092(0.010)
Kidney-L-Medulla	3.00±0.95	8.09±6.00(0.0023)	4.61±1.54(0.0015)	4.88±1.94(0.0018)
Kidney-L-Cortex	2.51±0.95	4.11±1.41(0.0007)	3.88±0.70(<0.0001)	4.30±1.64(0.0008)
Kidney-R-Medulla	2.96±0.97	8.74±5.98(0.0007)	4.31±1.55(0.006)	4.47±1.72(0.0053)
Kidney-R-Cortex	2.40±0.81	4.04±1.39(0.0004)	3.57±0.66(0.0001)	4.02±1.62(0.0015)
Liver	0.49±0.13	0.57±0.18(0.18)	0.58±0.087(0.029)	0.53±0.21(0.53)
Lung	0.16±0.041	0.22±0.039(0.0006)	0.19±0.042(0.042)	0.21±0.065(0.023)
Muscle	0.12±0.021	0.080±0.048(0.034)	0.059±0.020(0.28)	0.055±0.020(0.66)
Pancreas	0.43±0.13	0.54±0.26(0.19)	0.37±0.12(0.22)	0.34±0.12(0.070)
Skelton	0.12±0.021	0.16±0.027(0.0002)	0.14±0.024(0.012)	0.14±0.044(0.11)
Skin	0.12±0.039	0.14±0.034(0.17)	0.17±0.052(0.010)	0.24±0.068(<0.0001)
Spine	0.093±0.022	0.15±0.082(0.0089)	0.12±0.022(0.001)	0.12±0.04(0.036)
Spleen	0.25±0.095	0.54±0.20(<0.0001)	0.38±0.15(0.009)	0.40±0.29(0.058)
Stomach	0.15±0.084	0.20±0.068(0.068)	0.19±0.052(0.081)	0.17±0.12(0.55)
Testis-L	0.070±0.018	0.086±0.019(0.026)	0.089±0.027(0.027)	0.086±0.025(0.054)
Testis-R	0.068±0.025	0.089±0.018(0.005)	0.11±0.04(0.0028)	0.086±0.024(0.038)
Thymus	0.16±0.045	0.34±0.085(<0.0001)	0.20±0.033(0.0033)	0.057±0.011(0.035)

In vivo single-time point imaging studies – radioactivity uptake among tissues between nontreated control rats (n = 15) and rats treated with cyclophosphamide (n = 15), methotrexate (n = 15) or cisplatin (n = 15). The level of radioactivity uptake was determined from *in vivo* SPECT whole-body images acquired at 1 hour after the intravenous injection of ^{99m}Tc-duramycin. The absolute radioactivity uptake values in each tissue/organ in terms of %ID/voxel are shown as means ± standard deviations, with the *P* values included in parentheses. A *P* value of <0.05 is regarded as statistically significant.